

Simulations of multi-phase turbulence in jet cocoons

M. Krause* and P. Alexander

Astrophysics Group, Cavendish Laboratory, Cambridge CB3 0HE, UK

Accepted Received 2005 August 10

ABSTRACT

The interaction of optically emitting clouds with warm X-ray gas and hot, tenuous radio plasma in radio jet cocoons is modelled by 2D compressible hydrodynamic simulations. The initial setup is the Kelvin-Helmholtz instability at a contact surface of density contrast 10^4 . The denser medium contains clouds of higher density. Optically thin radiation is realised via a cooling source term. The cool phase effectively extracts energy from the other gas which is both, radiated away and used for acceleration of the cold phase. This increases the system's cooling rate substantially and leads to a massively amplified cold mass dropout. We show that it is feasible, given small seed clouds of order $100 M_{\odot}$, that all of the optically emitting gas in a radio jet cocoon may be produced by this mechanism on the propagation timescale of the jet. The mass is generally distributed as $T^{-1/2}$ with temperature, with a prominent peak at 14,000 K. This peak is likely to be related to the counteracting effects of shock heating and a strong rise in the cooling function. The volume filling factor of cold gas in this peak is of the order 10^{-5} to 10^{-3} and generally increases during the simulation time. The simulations tend towards an isotropic scale free Kolmogorov-type energy spectrum over the simulation timescale. We find the same Mach-number density relation as Kritsuk & Norman (2004) and show that this relation may explain the velocity widths of emission lines associated with high redshift radio galaxies, if the environmental temperature is lower, or the jet-ambient density ratio is less extreme than in their low redshift counterparts.

Key words: hydrodynamics – instabilities – turbulence – galaxies: jets – methods: numerical.

1 INTRODUCTION

Extragalactic radio jets have been observed to interact strongly with their environment. This is evident not only from their often fat radio cocoons but also from the cospatial optical and X-ray emission (detailed below). This is observational evidence for what is expected from theory, namely the co-existence of hot magnetised cocoon plasma, warm X-ray gas, and cold, possibly star forming clouds, all interacting with one another.

This article is particularly stimulated by observations of radio galaxies at a redshift of about one (e.g. Hippelein & Meisenheimer 1992; Meisenheimer & Hippelein 1992; Best, Longair, & Röttgering 1996; Best, Longair, & Roettgering 1997; Neeser, Meisenheimer, & Hippelein 1997; Best et al. 1998a; Best, Longair, & Roettgering 1998b; Best et al. 1999; Neeser, Hippelein, & Meisenheimer 1999; Best et al. 2000a; Best, Röttgering, & Longair 2000b,c; Best 2000; Inskip et al. 2002a,b, 2003, 2005). Clear trends are ob-

served: the smaller radio sources have the larger emission line regions, the greater line widths, and are more consistent with shock ionisation. This is further evidence for the tight connection between the gas phases present.

The traditional viewpoint has been to study the individual phases separately, analogously to interstellar medium (ISM) turbulence theory (Elmegreen & Scalo 2004). As for the case of the ISM, new insights can be expected from direct hydrodynamical simulation of the interaction. These interactions are so far unknown. The open questions include energy, momentum, and mass transfer between the phases. The origin of the cold phase is unclear (apart from the merger cases, compare Neeser et al. 1999): a common idea is that pre-existing clouds are activated for example by the bow shock or photo-ionised by a central quasar. A possible problem of this model might be the low visibility of clouds far from the radio emission, which would still be expected to be photo-ionised (Inskip et al. 2002b). It is rather unlikely that much of the cool gas is drawn from the host galaxy, because the solid angle occupied by the beam is quite small, and except at the very end of the jet the densest clouds are likely to pass through the contact surface into the cocoon,

* E-mail: M.Krause@mrao.cam.ac.uk

where the flow if anything moves the clouds back towards the galaxy (e.g. Alexander & Pooley 1996). Given the probably similar masses of warm and cold phase (see Section 2.3), it appears possible that the latter cooled and condensed from the former. This seems difficult for sources in nearby galaxy clusters, but may work at higher redshift, where the cluster gas is expected to be cooler, and therefore to have a shorter cooling time. Weak shocks caused by the jet may further lower the cooling time. This idea would explain the dependence of the appearance of cold gas on redshift (see Section 2.3).

A better understanding of these inter-relations would not only advance radio source physics, but bear the potential of using jets and the associated emission as probes of the surrounding (cluster) gas. As cluster gas properties at redshifts of one and beyond are still hard to determine with present day X-ray telescopes (e.g. Andreon et al. 2005), this may give important constraints, with implications for cosmology and galaxy formation.

We plan to address the problem in three ways. Here we concentrate on simulations that contain the three phases from the beginning and study their interaction in kpc-sized box simulations. Clues from large scale jet propagation and investigation of the possibility of condensing the cold phase entirely out of the warm one are deferred to future publications.

The three phases are reviewed individually in Section 2. Section 3 discusses the relation to turbulence research, the simulations are presented in Section 4 and discussed in Section 5.

2 THE THREE PHASES PRESENT IN RADIO GALAXIES

2.1 Hot magnetised radio plasma

Many of the more powerful FR II sources (Fanaroff & Riley 1974; Gilbert et al. 2004) possess fat radio cocoons. Provided the jets are light compared to the ambient gas, beam plasma that has passed the terminal shock region assembles in roughly cylindrical cocoons (e.g. Norman et al. 1982). According to momentum balance, the head advance speed v_h drops with the beam density ρ_j as:

$$v_h = \sqrt{\eta \epsilon} v_j, \quad (1)$$

where $\eta = \rho_j / \rho_0$, ρ_0 is the ambient density, v_j is the jet speed, and ϵ the model dependent thrust distribution factor (< 1). Therefore, the lighter the jets, the slower the head advance speed, and the wider the cocoons have to be in order to store the shocked beam plasma. Simulations still struggle to reproduce the observed cocoon widths, which at least in some cases require $\eta \lesssim 10^{-4}$ (Krause 2005), in agreement with analytical considerations (e.g. Alexander & Pooley 1996). The jet velocity must be a reasonable fraction of the speed of light – jet prominence (Hardcastle et al. 1999) and arm-length asymmetries (Arshakian & Longair 2004) suggest $v_j \gtrsim c/2$ whereas a bulk Lorentz factor of about 10 is suggested by X-ray–Compton studies (Tavecchio et al. 2004, and references therein) and the morphology and size of the bow shock in Cygnus A (Krause 2005). These conditions in the jet imply,

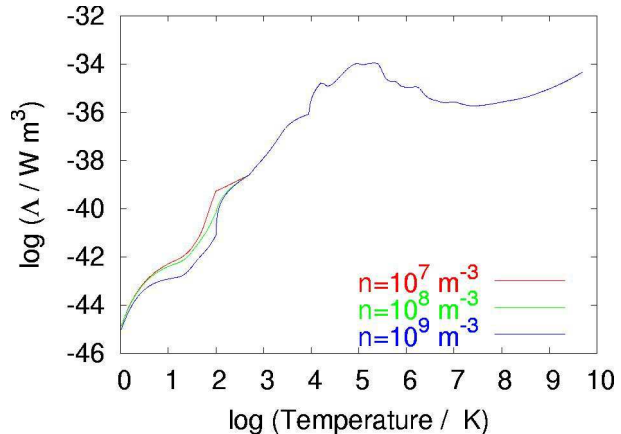


Figure 1. Employed cooling curve. The low temperature part is density dependent.

after the jet shock, a very hot tenuous cocoon plasma with an effective temperature of order

$$T_c = 3 \times 10^{11} \left(\frac{v_j}{c/2} \right)^2 \text{ K}. \quad (2)$$

2.2 Warm X-ray gas

The radio cocoons are in rough pressure equilibrium with the surrounding shocked X-ray gas at, typically, 10^7 – 10^8 K. Therefore, and for dynamical reasons (compare above) the typical density ratio between cocoon plasma and surrounding X-ray gas should be about 10^{-4} . The dividing contact surface is subject to Rayleigh-Taylor and Kelvin-Helmholtz instabilities, although it may be stabilised by deceleration (Alexander 2002; Krause 2005) and magnetic fields (Krause & Camenzind 2001) for some time. Hydrodynamic simulation indicates that a few percent of the gas mass pushed aside by the radio cocoon is entrained back into the cocoon region by these instabilities, typically of the order $10^9 M_\odot$ for sources of size 100 kpc (Krause 2005). This picture is confirmed by radio observations (e.g. Gilbert et al. 2004). While the regions close to the hotspots of FR II sources are usually sharply bound, indicating a stable contact surface, towards the centres the emission diffuses away and gets filamentary, indicating entrainment of the surrounding shocked ambient gas. The latter is very obvious from the high dynamic range observations of Cygnus A of Perley et al. (1984). The entrained X-ray gas has been resolved by Chandra observations of the same source (Smith et al. 2002). In the following, this will be called the warm phase in contrast to the hot, radio-emitting cocoon-plasma.

2.3 Cold emission line gas

A third gas component is revealed by the alignment effect (for a review see McCarthy 1993). Beyond a redshift of 0.6, optical emission is aligned with the radio jet and often copatial with the cocoon. This emission is indicative of comparatively cold ($T \approx 10^4$ K) gas. The emission is partly polarised to varying degree, which is interpreted as a scattering contribution of light from a hidden quasar by dust grains (e.g.

Solórzano-Iñarra et al. 2004, and references therein). Additionally, nebular emission (Inskip et al. 2002a,b) and newly formed stars (e.g. Best et al. 1996; Dey et al. 1997) may contribute to the continuum light (but see also Neeser et al. 1999). The emission line luminosity is well correlated with the radio power. Such a description sounds much like the ordinary inter-stellar medium (ISM) in galaxies. The ISM is traditionally regarded as a multi-phase medium itself. However, recent advances in turbulence research have revealed rapid transformation between clouds and inter-cloud medium, wherefore Elmegreen & Scalo (2004) drop the distinction. We adopt this viewpoint and regard all the gas that is able to cool significantly by emission on a reasonable time-scale (see below) as the third phase, which will be referred to as the cold phase.

Baum & McCarthy (2000) give a range of 10^8 – $10^{10} M_{\odot}$ for the cold gas component for radio galaxies at $z \approx 1$. This is likely to be much more than the radio plasma by a factor of at least a hundred, given the density ratio discussed above, and about the same as the entrained X-ray gas, as inferred from simulation.

3 CONNECTION TO TURBULENCE THEORY

'The appearance of instability in viscous shear flows usually results in the nonlinear outcome: the onset of turbulence' (Shu 1992, p 119). FR I jets have been recognised as turbulent flows early on (e.g. Bicknell 1984; Komissarov 1990). The cocoons of FR II jets are even more likely to be turbulent, since these shear flows probably have low velocities with respect to the surrounding shocked ambient gas. This has already been mentioned in the early simulation papers (e.g. Kössl & Müller 1988). The appearance of smaller and smaller vortices with increasing resolution has actually been observed in a resolution study by Krause & Camenzind (2001), who varied the resolution of their simulations by up to a factor of 40. Hence, the turbulent nature of the cocoons of FR II sources is evident, and the recent literature treats it as a matter of course (Saxton et al. 2002; Carvalho & O'Dea 2002).

An excellent review of interstellar turbulence can be found in Elmegreen & Scalo (2004). They point out that compressible turbulence, which is relevant here, is still not fully understood. For example, an inertial range where kinetic energy is transferred in a scale-free manner (the Kolmogorov law) to smaller scales (or larger scales as may be the case for 2D turbulence) is not expected a priori. The character of turbulence is furthermore dependent on magnetic fields and self-gravity. Since turbulence is a phenomenon which covers a wide range of physical scales, resolution in numerical simulations is an issue. In this paper we present simulations which while, by necessity, are of limited resolution, we believe offer improved physical insight. Some aspects of the problem we address have been studied by other authors (e.g. Kritsuk & Norman 2002, 2004; Mellema et al. 2002), thereby allowing some consistency check on our results.

Turbulence quickly decays, if not driven constantly. Its properties, however, may depend on the driving mechanism (Elmegreen & Scalo 2004). Many turbulence simulations use large scale driving by source terms. In the simulations pre-

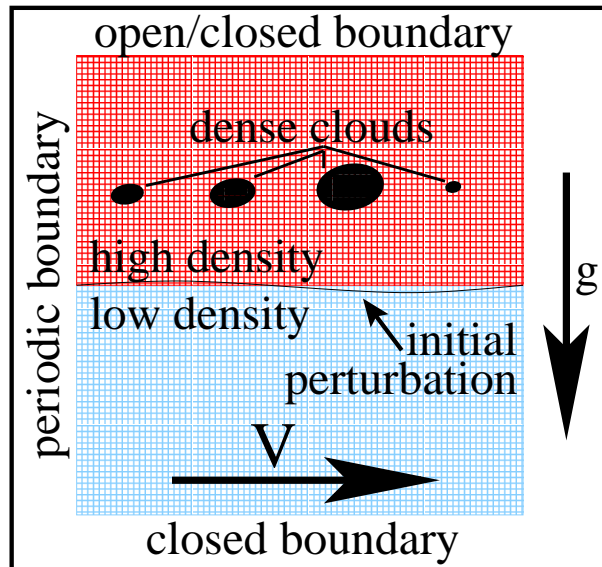


Figure 2. Sketch of the setup for all simulations. The three phases soon mix due to fluid instabilities, and form a turbulent region powered by the initial gravitational and kinetic energy.

sented below, the energy is initially stored mainly in kinetic energy, and transferred slowly to turbulent motions by the Kelvin-Helmholtz instability. Because the linear growth times of these instabilities depend on the length scale (Equations (6)), the driving starts on small scales and involves larger scales the longer the simulation is run for. This is designed to reproduce the conditions in jet cocoons as closely as possible, but it is different to most simulations in the literature.

There are a number of general results concerning compressible turbulence from theory and simulation which we expect to find reflected in our simulations. Turbulence theory finds log-normal density probability distribution functions (PDF) for isothermal turbulence (Elmegreen & Scalo 2004): power law tails are expected for specific heat ratios other than one. The volume filling factor as a function of density is determined to be a power law from simulation. The velocity PDF is expected to be Gaussian from analytic work but is found to be more exponential from simulations. In the cold phase, the average Mach number grows with density as $\bar{M} \propto \rho^{1/2}$ (Kritsuk & Norman 2004).

4 THE SIMULATIONS

Hydrodynamic simulations were performed in order to study the turbulent interaction of the three phases. The equations for mass (ρdx^3), momentum ($\rho \mathbf{v} dx^3$), and internal energy ($e dx^3$) are

$$\frac{\partial \rho}{\partial t} + \nabla \cdot (\rho \mathbf{v}) = 0 \quad (3)$$

$$\frac{\partial \rho \mathbf{v}}{\partial t} + \nabla \cdot (\rho \mathbf{v} \mathbf{v}) = -\nabla p - g \rho \quad (4)$$

$$\frac{\partial e}{\partial t} + \nabla \cdot (e \mathbf{v}) = -p \nabla \cdot \mathbf{v} - \frac{\rho^2}{m_p^2} \Lambda, \quad (5)$$

where m_p is the proton mass and the system is closed by the equation of state $p = (\gamma - 1)e$ with $\gamma = 5/3$ being the ratio of specific heats. These equations were evolved in two Cartesian dimensions with the code NIRVANA (Ziegler & Yorke 1997). This code is second order accurate in space and time, and is able to resolve shocks via artificial viscosity (compressible hydrodynamics).

Cooling is treated as a source term in the energy equation. The cooling curve was adopted from Basson (2002). For temperatures between 10^4K and $10^{8.5}\text{K}$, the Sutherland & Dopita (1993) cooling curve for solar metallicity was used. Above that temperature the cooling is due to bremsstrahlung: $\Lambda = 2.05 \times 10^{-40} \sqrt{T} (1 + 4.4 \times 10^{-10} T) \text{ Jm}^3/\text{s}$, where the second term in the bracket is the relativistic correction. For one run, the cooling curve was cut below 10^4 K , to emulate effects of photoionisation. For the others, cooling by collisional de-excitation of molecular hydrogen (Tegmark et al. 1997, 10^2K – 10^4K) and by emission lines from H_2 , HD, and CO molecules (Puy et al. 1999, $< 100\text{K}$) were included. This cooling curve is shown in Figure 1. Another source term is the constant gravity of $g = 10^{-10} \text{ m s}^{-2}$. The gravity does not influence the simulations by much but was included to make the simulations as realistic as possible.

We have also used the third order accurate Flash code, which is forced to conserve energy and momentum to check the results. We encounter numerical problems with both codes, when regions of hugely differing densities approach each other. This restricts the density ratios in the simulations. It turned out that, with given computational resources, we could perform better simulations with Nirvana. We could not reach enough resolution with Flash to produce reliable results in the parameter range of the presented Nirvana simulations. Therefore, we discuss mainly our Nirvana simulations.

4.1 Setup

The initial setup of the simulations is shown in Figure 2. The idea is to model the situation at the contact surface between jet cocoon and shocked ambient gas. The upper half of the computational square box of size $[1 \text{ kpc} \times 1 \text{ kpc}]$, resolved by $[512 \times 512]$ cells, is initially filled with gas of density $10^4 m_p \text{ m}^{-3}$. The pressure was set to decrease linearly with height, in order to achieve hydrostatic equilibrium. With a temperature of $2 \times 10^6 \text{ K}$, the cooling time is about 10 Myr, which is similar to our simulation time. Five elliptical clouds with a very high density (see Table 1) and various radii (0.008, 0.02, 0.04, 0.07, 0.004 kpc) have been placed in the high density region at a height of 0.6 kpc. This results in a total cold mass of 10^4 – $10^7 M_\odot \text{ kpc}^{-3}$. For determination of this density and similar ones to follow, the cells are assumed to represent cubes of three equal sides. Hence, the values are upper limits due to the unknown 3D structure. Observed emission line gas masses (see above) and radio cocoon sizes of about $V_{\text{coc}} = \pi r_{\text{coc}}^2 h \approx \pi (15 \text{ kpc})^2 100 \text{ kpc} \approx 3 \times 10^5 \text{ kpc}^3$ lead to cold gas masses of 10^3 – $10^5 M_\odot \text{ kpc}^{-3}$. We also include a control run without any clouds.

The lower half of the box contained low density gas ($m_p \text{ m}^{-3}$) at about the same pressure, which was adjusted experimentally for best numerical stability of the initial configuration. This gas was given an initial velocity of $v =$

$2 \times 10^7 \text{ m s}^{-1}$, corresponding to a Mach number of 0.8 (80) with respect to the gas in the lower (upper) part of the grid. The boundary is perturbed as a sine wave of amplitude 0.03 kpc. This excites Kelvin–Helmholtz instabilities, with a linear growth time of:

$$\tau_{\text{KH}} = 5 \text{ Myr} \left(\frac{\lambda}{1 \text{ kpc}} \right) \left(\frac{\eta}{10^{-4}} \right)^{-1} \left(\frac{v}{2 \times 10^7 \text{ m s}^{-1}} \right)^{-1}, \quad (6)$$

where η is the density ratio, and λ is the wavelength of the perturbation. The perturbations are seeded with a wavelength of the box size. However the discretisation seeds perturbations on the scale of the resolution, which dominates the evolution. The initial velocity is in the horizontal direction only, not parallel to the surface. As the smallest perturbations grow fastest, this speeds up the development towards turbulence. The gravitational acceleration is comparatively low, wherefore the linear Rayleigh–Taylor instability does not contribute significantly to the driving.

Simulation parameters that were varied between simulations are given in Table 1. Note that for the model with the temperature cut in the cooling function the cloud density was set to yield the minimum temperature.

The timestep was found to decrease substantially with contained mass. Hence the high mass simulation was stopped after 3 Myr.

4.2 General dynamics

We begin by discussing run 7c4 which serves to illustrate the dynamics shown in all simulations containing clouds (see Figure 3). At the beginning of the simulations, the dynamics is governed by the Kelvin–Helmholtz instability. There is also resonant a kink instability which could contribute in principle. This instability produces a characteristic shock pattern (a kinked shock) at the interface (Bassett & Woodward 1995). However, we have checked images of the velocity divergence, and could find no trace of this pattern. The evolving Kelvin–Helmholtz instability produces vortices in the subsonic lower half of the computational domain, and sends strong shocks into the upper medium and the clouds. Simultaneously, the clouds cool, either to the temperature cut of 10^4 K , or to about 10^3 K . In this phase, the clouds evolve much like the ones in the shocked cooling cloud simulations of Mellema et al. (2002). Once the shock passes, the clouds are compressed. Mellema et al. (2002) then see a fragmentation into small stable cloudlets: our simulations do not have sufficient resolution to observe fragmentation. Instead we observe the formation of one filament per cloud. When the contact surface reaches it, the filament spreads along the surface. The filament is initially unable to penetrate the contact surface due to the long Rayleigh–Taylor time-scale (Figure 3, second row, left). Subsequently, one of the clouds is stretched and pushed towards the upper boundary by a rising part of the instability. This particular feature is especially related to the numerical issues detailed in section 4.10. Another cloud, located at a declining part of the contact surface is reached by a branch of the low density gas and drawn into it (Figure 3, second row, right). There it is greatly stretched and soon forms a filamentary system. When the first of the dense filaments reaches the lower boundary (between the centre and the right plots of the bottom row in Figure 3) the structure of the flow changes. The low density

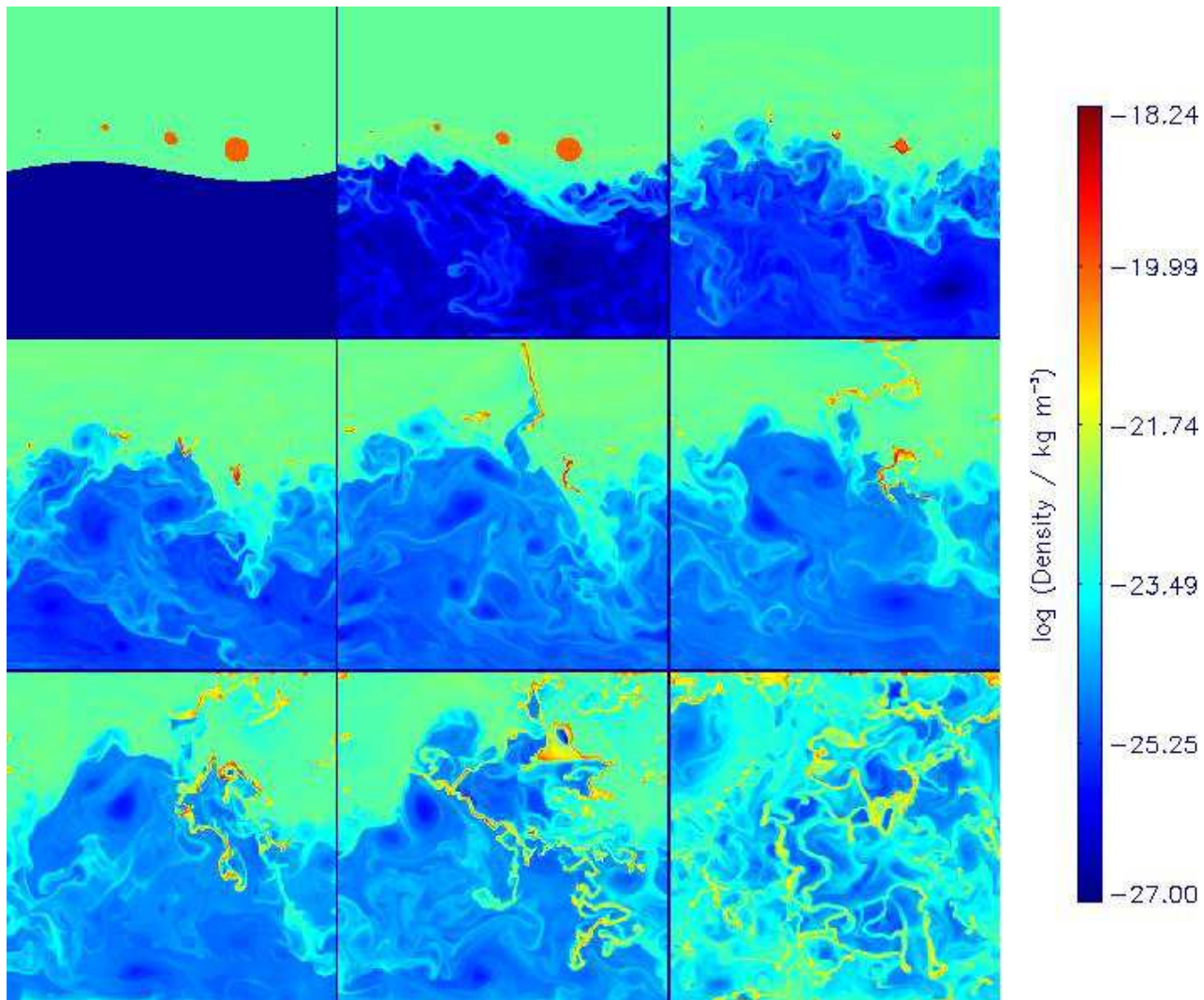


Figure 3. Logarithmic density plots at nine representative simulation times (0, 0.2, 0.9, 1.7, 2.4, 3.2, 4.1, 4.8, and 7.7 Myr) for RUN 7c4.

Table 1. Simulation parameters

| Label | Cloud density [$m_p m^{-3}$] | Total cloud mass [$M_\odot kpc^{-3}$] | Upper boundary | Temperature cut [K] | Final time [Myr] |
|-------------------|-----------------------------------|--|----------------|------------------------|---------------------|
| ctrl ^a | 10^4 | 1.5×10^3 | closed | 0 | 10 |
| 5c0 | 10^5 | 1.5×10^4 | closed | 0 | 10 |
| 6o0 | 10^6 | 1.5×10^5 | open | 0 | 10 |
| 7c4 | 5×10^6 | 7.4×10^5 | closed | 10^4 | 10 |
| 7o0 | 10^7 | 1.5×10^6 | open | 0 | 10 |
| 7c0 | 10^7 | 1.5×10^6 | closed | 0 | 6.4 |
| 8o0 | 10^8 | 1.5×10^7 | open | 0 | 3 |

^a contains no clouds, just background density

gas can no longer rush through from left to right, and the motions turn completely into turbulence. Towards the end, the upper part moves left and the lower one to the right, forming one large scale vortex.

4.3 Dynamics of the different setups

Logarithmic density plots at 3 Myr are shown in Figure 4 for all six simulations containing clouds. The mass loading clearly affects the evolution of the Kelvin-Helmholtz instability. This is most evident when comparing the right column

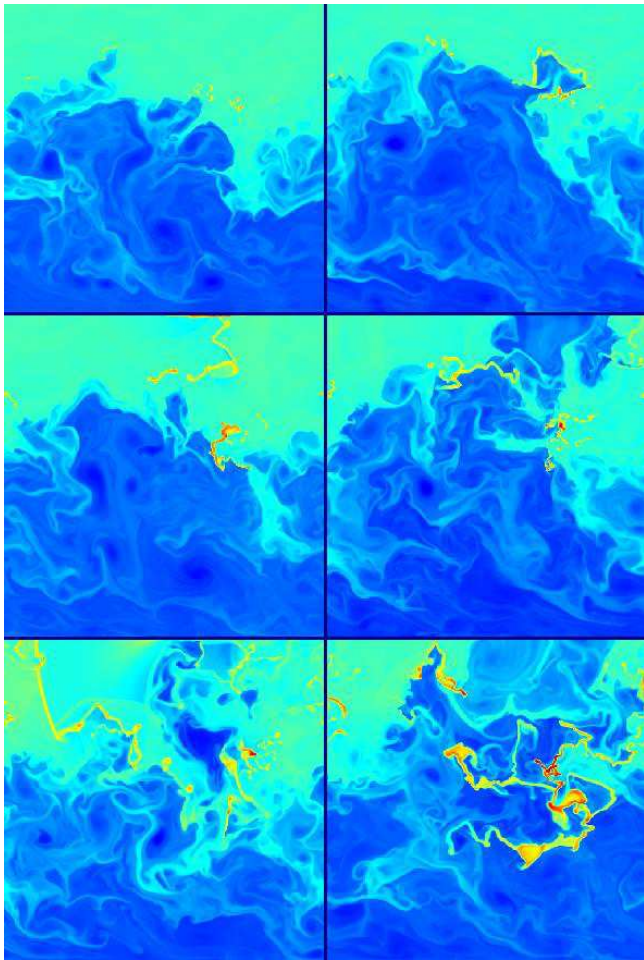


Figure 4. Logarithmic density plots at 3 Myr for all the simulations with clouds in the order of Table 1 (5c0: top left, 6o0: top right, 7c4: middle left, 7o0: middle right, 7c0 bottom left, 8o0: bottom right). An open upper boundary (right plots) amplifies the Kelvin-Helmholtz instability. More cold mass (towards the bottom) speeds up the formation of filaments.

of Figure 4 (open upper boundary). When the first filament is stretched towards the upper boundary, the low density gas flows along, leaving the grid if the upper boundary is open. In the simulations with lower cloud density, this feature is suppressed, and the low density gas stays in the lower part of the computational domain. Also for the simulations with lower initial cloud mass the overall evolution is slower.

The direct comparison between open and closed boundary (runs 7c0 and 7o0) shows that dense gas assembles near the boundary for the closed simulations and that this gas leaves the grid for the open ones. This is not compensated by inflows, and hence, the open boundary cases have less cold mass than the closed upper boundary simulations.

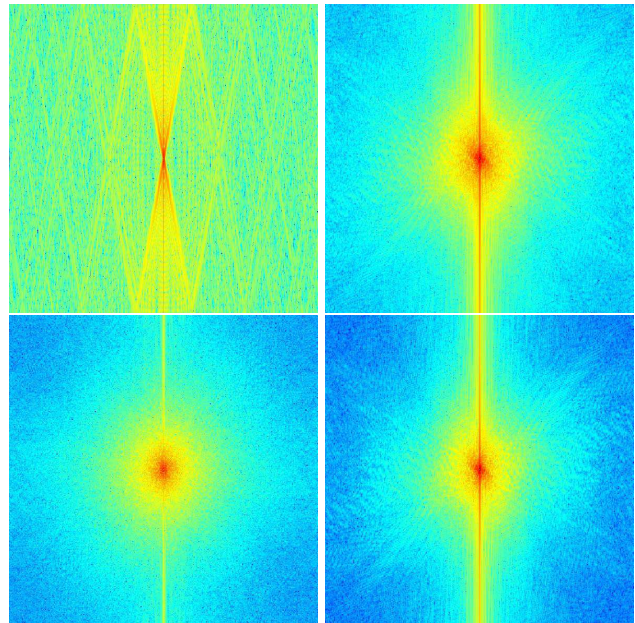


Figure 5. Two-dimensional velocity power spectra for run 7c4 at 0.2 Myr (top left), 3.2 Myr (top right), and 7.7 Myr (bottom left) and for run 7o0 at $t = 7.7$ Myr (bottom right). The power spectra are evaluated in the zero momentum frame. Wave-vector zero is at the centre.

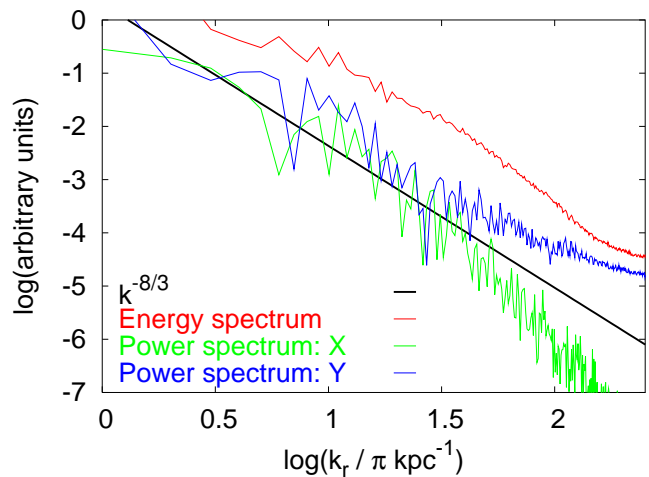


Figure 6. Energy spectrum $(E(k_r)dk_r = \int_{k_\phi} P(k_r, k_\phi)k_r dk_\phi dk_r)$, X- and Y-cuts through the power spectrum of run 7c4 at 7.7 Myr. The large scales isotropise first, showing a Kolmogorov-like decline ($k^{-8/3}$ in the power spectrum cuts, corresponding to $k^{-5/3}$ in the energy spectrum). The smallest scales do not isotropise up to the end of the simulation, which is due to the bar feature.

The temperature cut results in a significantly reduced maximum density (by a factor of order 10). The densest cloud occupies a bigger area, i.e. it is less condensed. Also, the aforementioned uplifting of low density gas is suppressed.

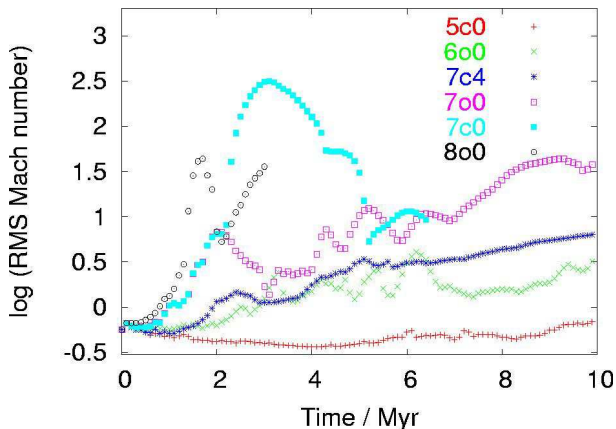


Figure 7. Root mean squared Mach number versus time for all runs with clouds. The Mach number generally grows with time. The simulations with higher mass load have higher average Mach numbers. The high amplitude features are due high density filaments hitting a boundary, and are especially pronounced for closed boundaries..

4.4 Power spectrum

For comparison to turbulence studies, it is important to check isotropy and scale-dependence. Therefore, we examined the power spectrum of the velocity,

$$P(\mathbf{k}) = \sum_{i=x,y} \left| \int_{\text{box}} v_i e^{i\mathbf{k}\cdot\mathbf{x}} d^2x \right|^2.$$

We use velocities in the zero momentum frame although the results do not depend on that particular choice. Two-dimensional representations of the power spectrum are shown in Figure 5. The behaviour for the different runs is very similar. Hence, only results from runs 7c4, and 7o0 are shown. Even the early power spectra look quite isotropic, apart from a horizontal bar feature. However, the energy spectra up to a few million years are dominated by the bar feature, which produces power law indices around -2 . Large scales isotropise first, and at 7.7 Myr, we find a Kolmogorov-like isotropic power spectrum for most scales (Figure 6). The bar feature varies in strength, but is generally decreasing. The open upper boundary simulation showed a stronger feature at the same time. The same is true for simulations with less cold mass load.

We conclude that for larger scales, isotropic, Kolmogorov-like turbulence is essentially reached after a few million years of simulation time. Some anisotropy remains on small scales.

4.5 Mach number, density and pressure distributions

The root mean squared (rms) Mach number is shown in Figure 7. It is generally well above one with the exception of run 5c0.

The choice of boundary condition has a big impact on the rms Mach number. We compare the three simulations with roughly the same initial density (7o0,7c0,7c4). The big bump in the 7c0 line is produced by one large filament hitting the upper boundary. The latter releases so much kinetic energy that the rms Mach number reaches up to a factor of

ten larger than in the open boundary case for the same density. Remarkably, after relaxation, the two simulations rejoin the same path. The bump is completely damped in the simulation with the temperature cut (7c4). The temperature cut reduces the peak values of the density, which leads to the more modest interaction with the grid boundary.

The most evident feature in Figure 7 is the constant rising of the rms Mach number and the dependence on the mass loading. More cold mass results in higher rms Mach numbers. This observation can be explained by a remarkable relationship between the density and the Mach number.

The relationship between density and Mach number is shown in the 2D-histograms of Figure 8. These diagrams display the volume occupation of gas at a given density and Mach number. We have chosen the time of 3 Myr (10 Myr) for the higher (lower) cold mass load simulations, because the turbulence is well evolved at that time, with the mixing between the low and medium density gas still being acceptably small. These plots look very similar at most other simulation times. Mixing of these gas phases is indicated by the two peaks that are initially at $10^{-27} \text{ kg m}^{-3}$ and $10^{-23} \text{ kg m}^{-3}$ coming closer together.

Between these densities, the Mach number is independent of the density. Since the simulation is effectively isobaric at those densities (see Figure 9), this means that the kinetic energy density is roughly constant, indicative of a quasi-equilibrium state. The same relation would be expected in a shock dominated scenario, where $T \propto v^2$. At high densities, the internal energy is reduced by the radiation losses, which increases the Mach number. Although this can change the pressure by many orders of magnitude in individual cells, the bulk of the material can compensate for the pressure loss by contraction and shock heating, which brings the gas back to near isobaric conditions. Since the velocity is not correlated with the density, the dependence of the Mach number on density ($M^2 = \rho v^2 / \gamma p$) is dominated by the explicit density dependence. These findings agree well with the 3D simulations of Kritsuk & Norman (2004) who drive the turbulence by the thermal instability, only, and do not include the low density phase.

The $M \propto \rho^{1/2}$ branch has got a higher occupation and extends to higher Mach number for higher mass loading and later simulation times. This causes the behaviour of the rms Mach number in Figure 7.

Typical pressure versus density histograms are shown in Figure 9. Although the occupied phase space spans many orders of magnitude in both dimensions, the pressure is remarkably peaked towards a central value, even in regions with high density and a shorter cooling time – here the pressure is, in general, at most a factor of ten below the low density gas. The prominent linear features in these figures are due to two processes. One is quasi-adiabatic expansion and compression of the marginally cooling gas at $10^{-23} \text{ kg m}^{-3}$, which initially fills the most of the upper part of the grid. The other is the quasi-isothermal regime at the prominent drop of the cooling function at about 10^4 K . The line is most prominent in the simulation with the cut in the cooling function but is also apparent in the other simulations at a temperature of about 14,000 K. Evidently, at this point the energy gain due to shocks caused by the turbulent motions balance the radiation losses.

The density PDFs are dominated by a power law be-

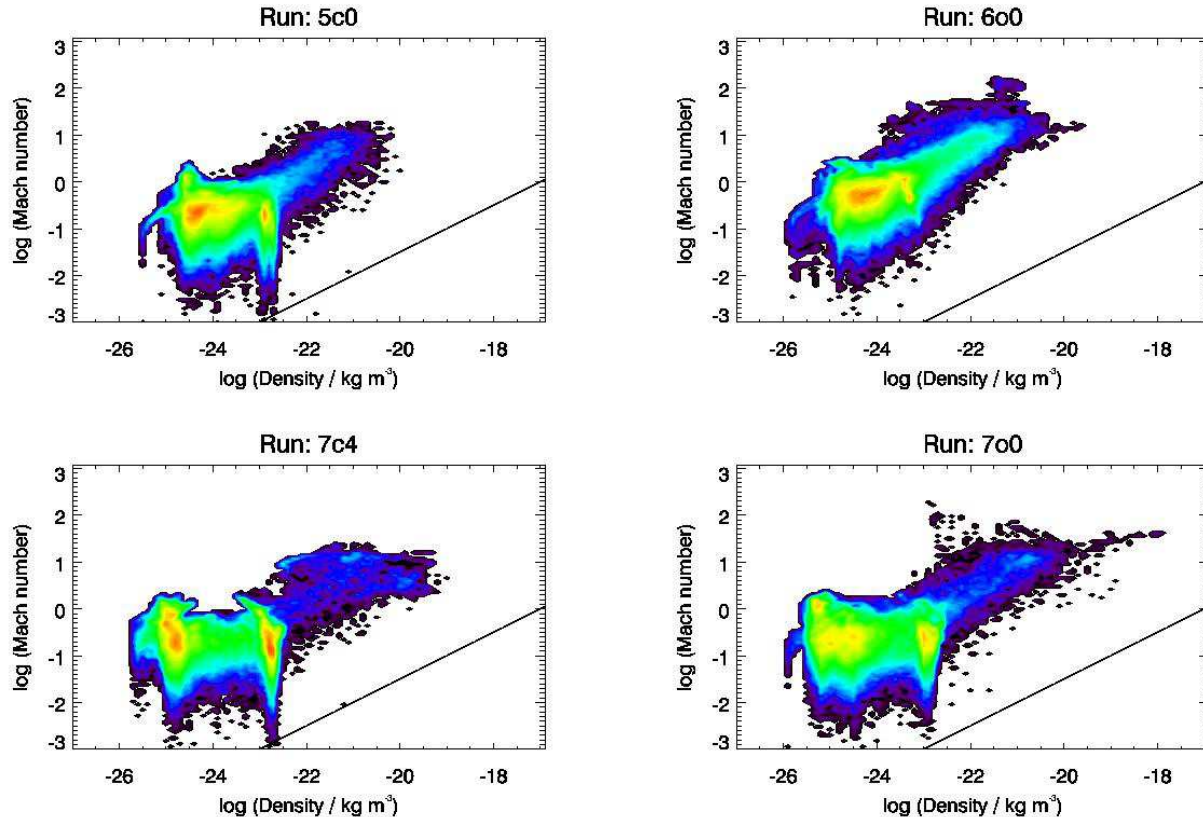


Figure 8. Phase diagrams showing the logarithmic volume occupation at a given density and Mach number for runs 5c0 and 6o0 (top at 10 Myr), and runs 7c4 and 7c0 (bottom at 3 Myr). The distribution is bimodal: low density gas is unable to cool and forms a turbulent system where the Mach number distribution is independent of the density. Gas with short cooling times joins at a density of about 10^{-23} kg m^{-3} and its Mach number grows roughly with the square root of the density. The fiducial line indicates a $M \propto \rho^{1/2}$ dependence. Colour coding is the same as on other figures.

haviour (Figure 10). As long as the peaks of the initial condition remain visible, the region between the peaks tends to follow a $V(\rho) \propto \rho^{-1/2}$ law, where $V(\rho)$ is the occupied volume at a particular density ρ . The high density part of the distribution reflects the mass loading, and is independent of the low density part. This region also follows the $\rho^{-1/2}$ law, at least for higher mass load. Over time, the region around 10^{-22} kg m^{-3} becomes more and more populated. As the peaks diffuse, the distribution becomes uniform with exponential type cutoffs towards low and high density.

4.6 Temperature distribution

We show the distribution of gas mass as a function of temperature in Figure 11. The general behaviour is well described by a $dM/dT \propto 1/\sqrt{T}$ law. The high temperature part ($T > 10^6$ K) evolves independently from the cooler part. Due to numerical mixing, the upper temperature of the gas moves to lower temperature keeping an exponential-type cutoff. In all simulations, the distribution evolves quickly to follow a $dM/dT \propto 1/\sqrt{T}$ form for $T > 10^6$ K up to the cutoff. There is a well defined peak at $T \approx 10^6$ K which broadens during the simulation. For $T < 10^6$ K the distribution evolves more slowly towards the same $dM/dT \propto 1/\sqrt{T}$ established at higher temperatures and at a rate which in-

creases with initial cloud mass. A peak at 14,000 K is well-defined in all simulations, and does not evolve with time. Below $\approx 10^3$ K the distribution evolves to form what may be a power-law decline at low temperatures.

4.7 Filling factor and mass

NIRVANA conserves the total mass to machine accuracy. In the simulations with closed boundaries, the mass is therefore constant (Figure 12, right). The other simulations lose up to about 50 per cent of the mass over the grid boundary – the ordering according to initial mass loading is essentially maintained throughout the simulation.

Since radiation transfer is not included into the simulation, the ionisation structure and nebular emission properties cannot be deduced in detail. However, from the strong drop of the gas mass towards higher temperature (Figure 11), and the drop of the cooling function towards lower temperature, it is clear that the gas with a temperature close to 14,000 K is responsible for much of the optical luminosity. In Figure 12 (left) we show the volume filling factor of gas with temperature $14,000 \pm 2,000$ K, which corresponds to the peak in the mass versus temperature distribution in Figure 11. This filling factor depends mostly on mass, with the three most accurate simulations (5c0, 6o0, and 7c4, see

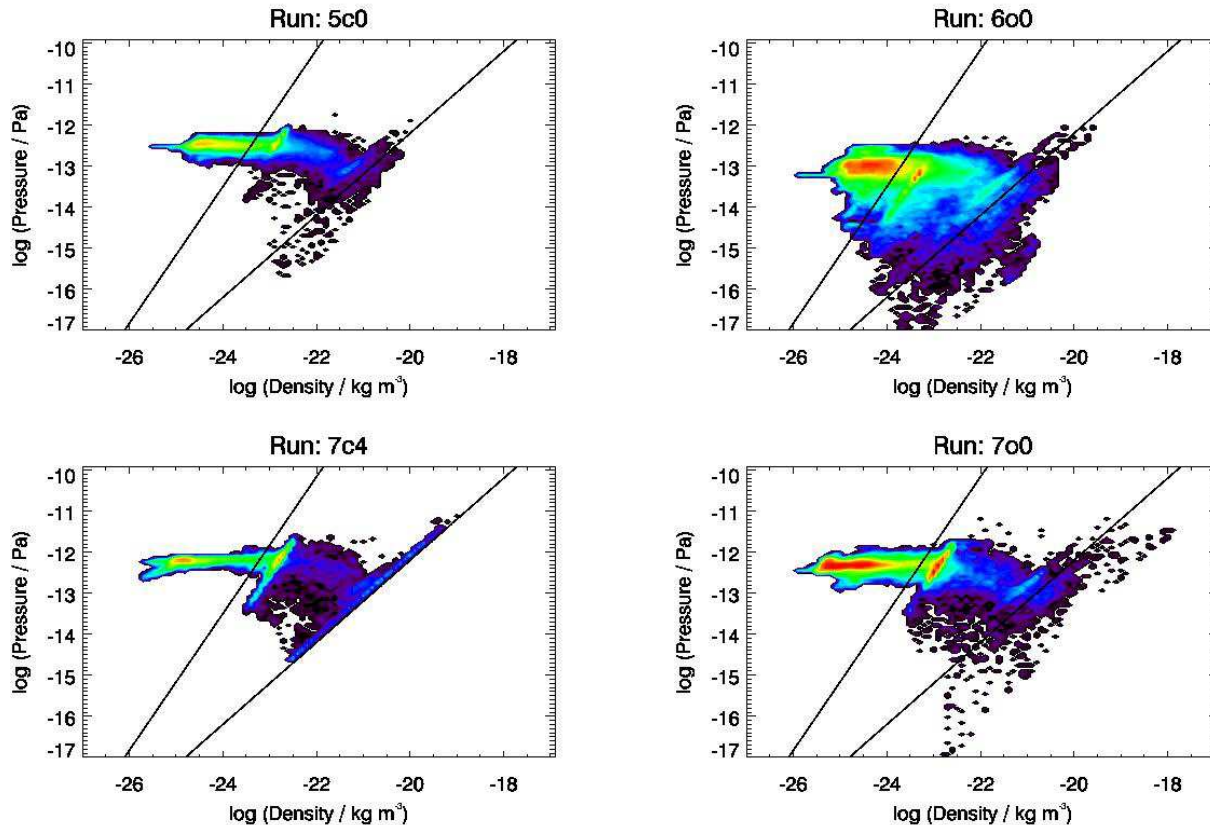


Figure 9. Phase diagrams showing the logarithmic volume occupation at a given density and pressure for runs 5c0 and 6o0 (top at 10 Myr), and runs 7c4 and 7o0 (bottom at 3 Myr). The pressure of much of the simulated volume is within a factor of a few, even in the strongly radiating part. Fiducial lines of slope 5/3 and 1 highlight adiabatic expansion features, prominently around a density of 10^{-23} kg m^{-3} (upper background gas), and isothermal components, respectively. In run 7c4, the 10^4 K line marks the border of the accessible phase space, in the other simulations, gas assembles at a slightly higher temperature due to the drop of the cooling function. Colour coding is the same as on other figures.

Section 4.10 below) following nearly parallel paths. As expected, higher initial mass loading results in a higher filling factor. For most of the simulation times, the filling factor stays between $\approx 10^{-3}$ and $\approx 10^{-2}$. Since these are 2D simulations, this would correspond to a volume filling factor of between 10^{-5} and 10^{-3} in 3D, assuming similar structuring in all dimensions.

4.8 Energy loss

Energy conservation is not guaranteed formally by the numerical method employed by NIRVANA. However, for practical considerations, it is usually conserved to reasonable accuracy, given sufficient resolution. This is the case for at least three of our runs (ctrl, 5c0, and 6o0, see Section 4.10 below for further discussion) – we therefore first focus on the energy evolution of these three simulations. Figure 13 (top left) shows the time evolution of the total energy for all runs, including the control run. Since there are no energy sources in the simulated volume, the total energy should monotonically decrease, at least in the closed box cases, due to the radiation term. In the control run without clouds the system loses energy at a nearly constant rate of 4×10^{28} W. For the simulation with the lightest clouds, the rate increases to

18×10^{28} W, and for run 6o0, the total cooling increases further to 22×10^{28} W. As might have been expected, the presence of the cool clouds increases the cooling rate. This is no longer evident for the simulations with higher mass loading. While at later times they turn to monotonic energy decrease at an even greater rate, they are obviously dominated by numerical effects for some and in the case of run 8o0 even much of the simulation. These numerical errors can be traced back to the kinetic energy. While the thermal energy (Figure 13, bottom left) shows essentially a smooth energy decline, with the only significant dependence being on mass in the expected way, the kinetic energy displays strong and artificial wiggles, which is discussed below. The extraction of energy from the high temperature system can be seen in yet another way. The fraction of energy in gas hotter than 10^6 K is shown in Figure 13 (top right). The system not only loses energy faster with increasing mass loading, but additionally energy is increasingly found in the low temperature gas.

4.9 Cold mass dropout

The increased system cooling rate due to the cold mass content leads to amplified mass dropout – this is illustrated in

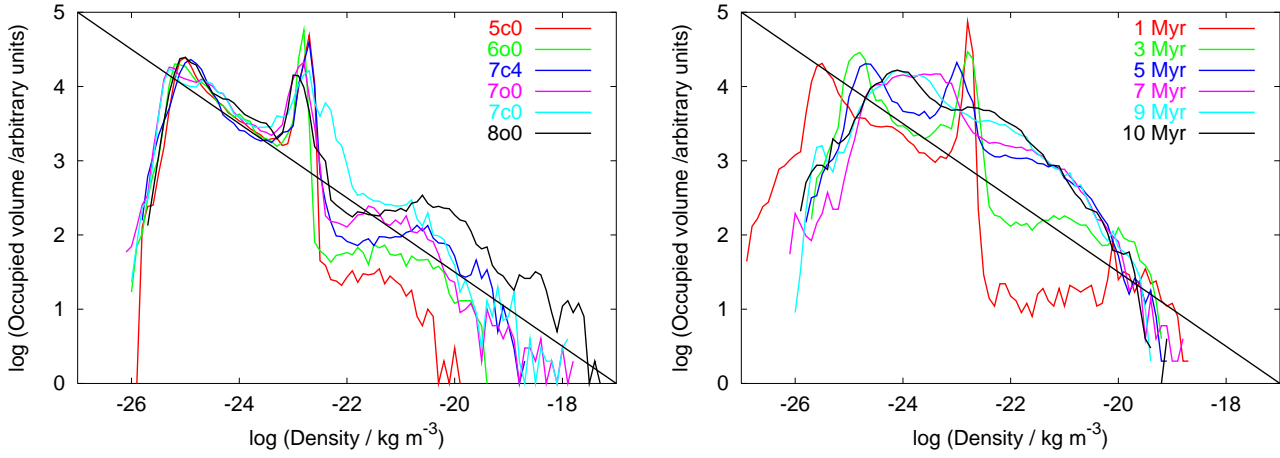


Figure 10. Left: Density probability distribution functions at a representative time of 2.5 Myr for all simulations. The fiducial line is proportional to $\rho^{-1/2}$. Right: The same for run 7c4 for a series of simulation times.

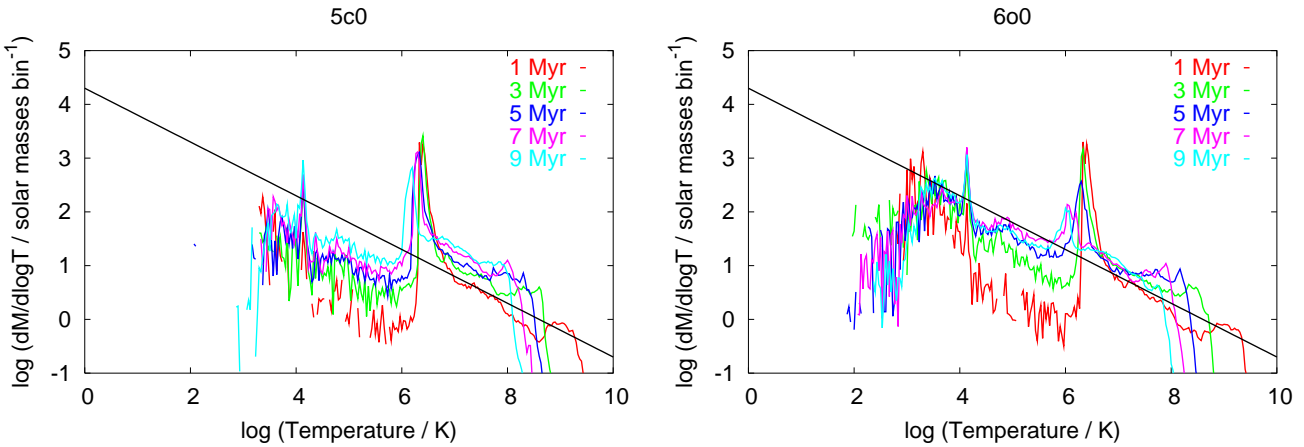


Figure 11. Gas mass distribution versus temperature for runs 5c0 and 6o0 at different simulation times. The black line is proportional to $1/\sqrt{T}$. The size of the temperature bins was 0.03.

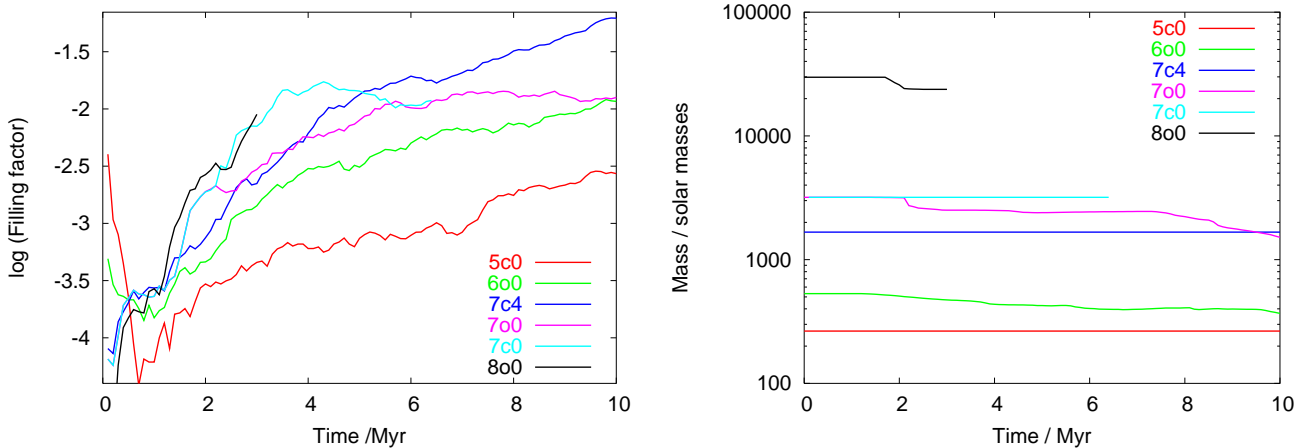


Figure 12. Filling factor (left) of gas in the 14,000 K peak and total mass (right) over time for all simulations with clouds. The mass is conserved by NIRVANA, and therefore, only the simulations with open boundary lose some mass (up to $\approx 50\%$)

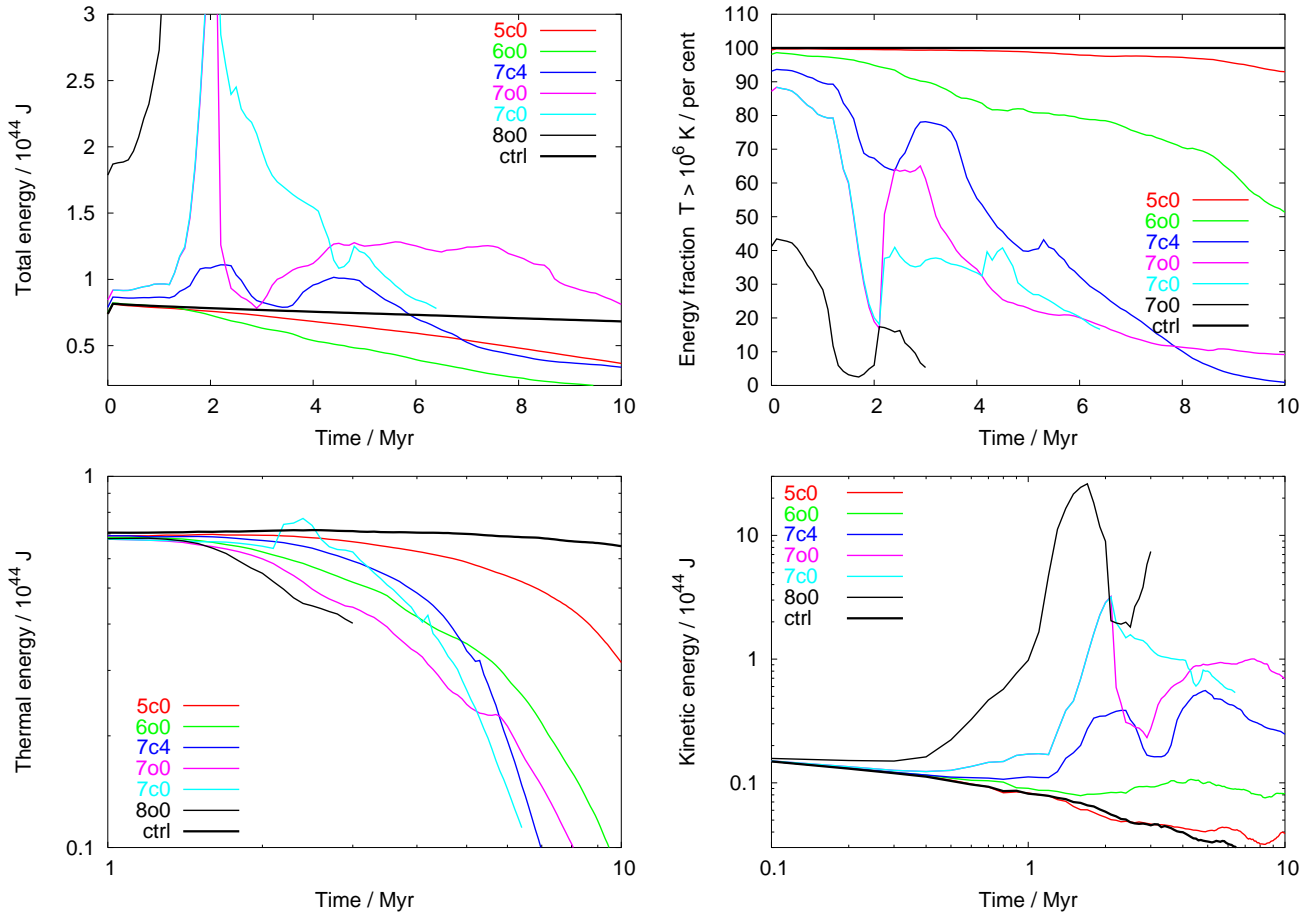


Figure 13. Energy evolution over time for all runs. Top left: total (i.e. thermal, kinetic and gravitational) energy; top right: fraction of total energy in gas hotter than 10^6 K; bottom left: thermal energy; bottom right: kinetic energy. All runs besides ctrl, 5c0 and 6o0 show problems with energy conservation (see text), which can be traced to the kinetic energy.

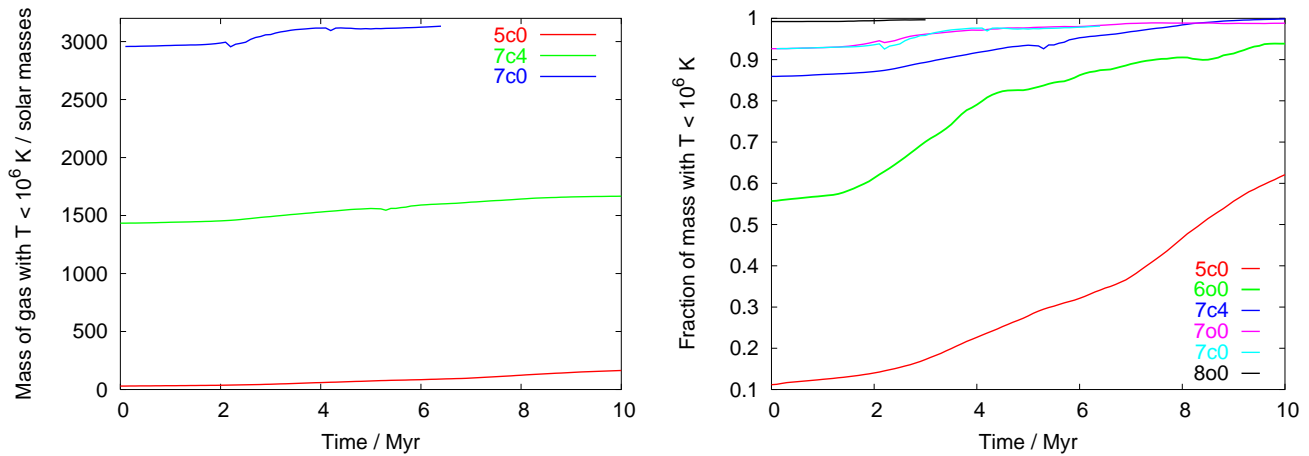


Figure 14. Time evolution of the cold gas phase ($T < 10^6$ K) for cloud containing simulations. Left: total amount of cold gas for the simulations with closed boundary. Right: Evolution of the cold gas mass fraction for all simulations. In the control run, no cold gas was detected over 10 Myr.

Figure 14. As discussed in Section 4.7, the total mass is conserved in the closed boundary simulations. The cold mass is therefore increased by dropout from the warm phase, only. In the control run, there is no cold mass present initially, and none drops out during the simulation time. Runs 5c0, 7c4, and 7c0 start with a cold mass of 30, 1434, and 2957 M_{\odot} , respectively: they gain cold mass at rates of 13.4, 23.3, and 27.3 $M_{\odot} \text{ Myr}^{-1}$, on average. The higher mass loaded simulations are limited by the available mass. At the beginning of the simulation, their cold gas mass is already ≈ 90 per cent of the total mass. They gain almost all of the rest during the simulation time. The cold mass evolution for run 5c0 can be well fitted by an exponential growth with e-folding time of 6 Myr. This corresponds to a simple interpretation in which the rate of mass dropout is proportional to the mass of cold gas. We note that runs 7c0 and 7o0, which differ only in their boundary condition, have very similar cold gas mass fraction histories, suggesting that the boundary conditions are unimportant for the fractional mass dropout. This is confirmed by the similar shape of all the curves in Figure 14 (right). The simulations with small initial cold gas mass fraction show increasing growth up to about 80 per cent. Further growth proceeds in a linear fashion.

4.10 Numerical issues

As indicated above in Section 4.8, the higher mass loaded simulations show increasing problems with energy conservation, in particular kinetic energy. Careful inspection of the simulations showed that the velocity errors depend strongly on the density contrast between cells. In the high mass loaded simulations, as soon as the very light gas in the lower half of the simulations comes into contact with the high density clouds, high velocity errors result. This is most evident in the total and kinetic energy plots (Figure 13). The higher the initial density, the higher the numerical error. Simulations 5c0 and 6o0 show no indication of the problem. Run 7c4 shows moderate errors. Runs 7o0 and 7c0 display moderate errors with a singular spurious event around 2 Myr. The fact that 7c4 shows only moderate errors at this time determines the critical density contrast to be about 10^7 . Run 8o0 is dominated strongly by numerical errors for much of the simulation time. We have checked that these errors decrease, as expected, if the numerical resolution is increased. Some aspects of the simulations are affected worse than others. Regarding most of the results discussed so far, a noticeable similarity and continuation of the results argues for the kinetic energy errors not to have a too large effect. In particular, the power spectrum is completely unaffected. Comparison of the phase diagrams for runs 7o0 and 7c0 shows that once the gas which was accelerated in the singular spurious event has left the grid (7o0), the diagram soon reverts to normal, in contrast to the closed boundary simulation (7c0). The high mass load simulations give the best signal to noise in the phase diagrams. However, because of the energy conservation issue, we include run 8o0 only to demonstrate the limitation of the method most clearly, and base our conclusions exclusively on the very best results.

A further check we have performed was to repeat the simulation with the FLASH code (Fryxell et al. 2000; Calder et al. 2002), which guarantees energy conservation. However, in this case another problem appeared in low reso-

lution runs. Here, the clouds were soon surrounded by a low pressure shell of a width equal to the resolution limit, which seriously damped the propagation of shocks into the clouds. The clouds essentially kept their shape for long times, even if accelerated. This problem could be solved by going to very high resolution, which corresponds for regions of smooth flow roughly to a four times better resolution compared to the simulations presented above, due to the higher order scheme of FLASH. We also adjusted the setup to have a single more massive cloud and allowed for higher background density (top: $10^5 m_p \text{ m}^{-3}$, bottom: $10^2 m_p \text{ m}^{-3}$). With such a setup we obtain very similar results to the NIRVANA simulations (see Figure 15). The cloud soon collapses to form a filament, dispersing into little cloudlets afterwards. The Mach-number density relation is consistent with the NIRVANA results, and the gas mass versus temperature distribution shows the same general behaviour and structure.

4.11 Velocity distribution functions

The velocity PDFs for the two most reliable runs (5c0 and 6o0) are shown in Figure 16. As expected from general turbulence theory, they show a Gaussian core with signs of acceleration due to drag and upwards driven shock waves towards positive velocities. These two most trustworthy simulations also show a dependence of the width on the mass loading. This confirms the earlier findings that in the simulations with higher mass load, the fraction of kinetic energy in the cold phase rises faster.

5 DISCUSSION

We present simulations of the Kelvin-Helmholtz instability with clouds of differing density. The clouds are shocked, collapse into a filament, and then disperse into cloudlets and more filaments. There is no indication of the cold mass being heated beyond typical emission line gas temperatures. On the contrary, over time more and more gas condenses into the cold phase.

Scale-free turbulence is established on the larger scales first. The smallest scales remain anisotropic up to the end of the simulation

In general, the rms Mach number increases during the simulation. This is due to the cold gas acquiring high velocities. In particular, for gas with longer cooling time, the Mach number is independent of the density, whereas for strongly cooling gas, the Mach number is proportional to the square root of the density. The latter dependency is identical to the one found by Kritsuk & Norman (2004).

The density probability distribution function shows a power law behaviour between the peaks imposed by the initial distribution, $P_{\rho}(\rho) \propto \rho^{-1/2}$. A similar behaviour is seen in the gas mass versus temperature plots. Generally, the distributions follow $M(T) \propto T^{-1/2}$, with the region between 10^4 K and 10^6 K evolving gradually over a few million years to follow the same scaling as at high temperature. But what is the cause of this behaviour? Because of the roughly constant pressure, the entropy distribution is also a power law. This rules out adiabatic processes. We are left with shock heating, cooling and mixing. Cooling and shocks contribute little for the gas with $T > 10^6 \text{ K}$. So, mixing seems

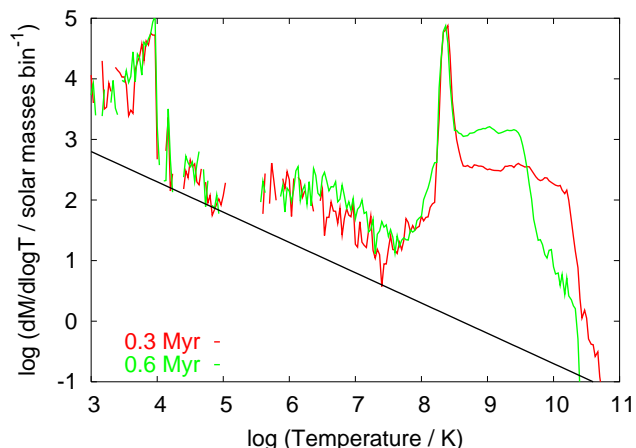
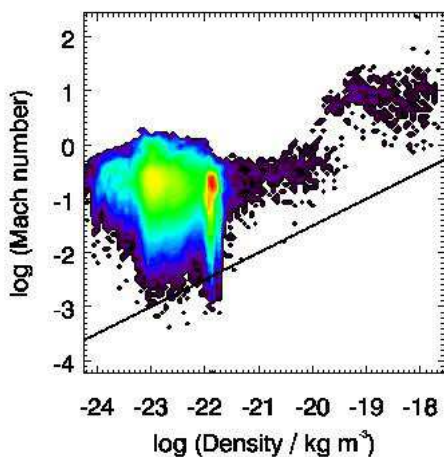
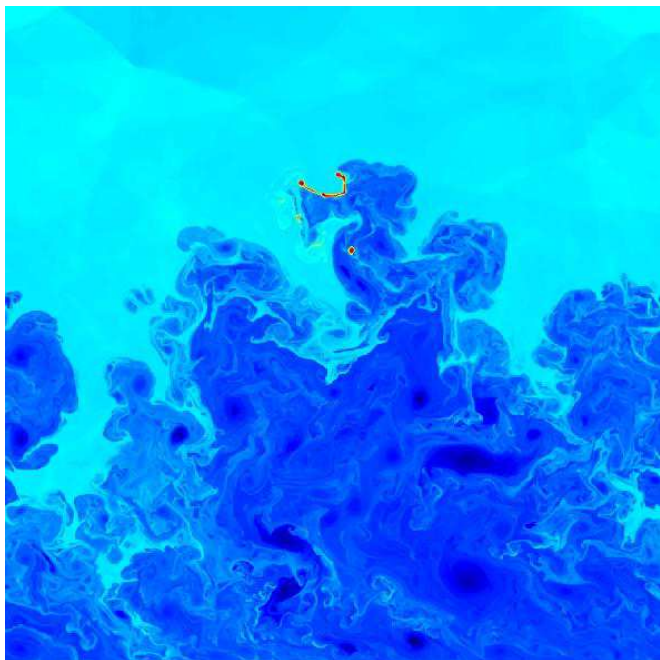


Figure 15. Selection of results for the validation run with FLASH. Top: logarithmic density distribution at 1 Myr, middle: density Mach number histogram at 1 Myr, bottom: gas mass over temperature, all gas, bottom right: gas mass over temperature between 5,000 K and 30,000 K, staggered for 13 timesteps from 0.1 Myr to 1.3 Myr.

to be the best explanation for the power law slope of the distribution functions of density and temperature. Mixing is inevitable in multi-phase turbulence simulations. In reality, mixing is likely to occur at a lower level, consequently the enhancements over the mixing distributions should be more pronounced. There is a worry that the peak around 14,000 K described in the following might be entirely due to the mixing. Against this possibility argues:

- The peak builds up early, when the mixing in the cold gas is still at low level.
- The 14,000 K peak joins the lower temperature gas above the mixing power law.
- The much less diffusive Flash simulation, produces a very similar peak.

We conclude that the 14,000 K peak is probably unaffected by the mixing.

This peak is in fact likely to be due to shock heating combined with the effects of the steep cooling curve. The peak appears in all simulations at most times. Since there is a drop in the cooling function towards lower temperature and there is a drop in gas mass towards higher temperature, the gas close to this temperature may contribute most of the optical emission. Its filling factor depends on the initial mass loading, and corresponds to 10^{-5} to 10^{-3} , for a realistic 3D generalisation. The velocity of this gas is distributed like a Gaussian in run 5o0. Run 6c0 has a pronounced deviation on the positive side due to acceleration, and appears unrelaxed. The typical width of observed emission lines may be understood by the Mach-number density relation. Gas with low cooling time was shown to have $M \propto \sqrt{\rho}$, i.e. the velocity is constant. This is valid for gas of a temperature up to $\approx 10^6$ K. For hot gas, the Mach number is constant, i.e. the velocity drops with $\rho^{-1/2}$. The hot radio plasma, has velocities of typically 10^5 km s $^{-1}$ when entering the cocoon, which will become increasingly turbulent. If the entrained ambient gas is roughly 10,000 times denser, it would be accelerated to typical velocities of 1000 km s $^{-1}$. If in $z \approx 1$ radio galaxies that gas has a temperature of $\gtrsim 10^7$ K as for nearby sources, then gas with $T < 10^6$ K would have a typical velocity width of a few 100 km s $^{-1}$. However, the typical observed velocity width is ≈ 1000 km s $^{-1}$. Hence, either the density ratio in these sources is typically less extreme than assumed here, or the typical temperature of the ambient gas is below 10^7 K (for both, a factor of ≈ 10 would suffice).

Excess cold mass is located in a broad peak around 10^3 K, which would contain substantial amounts of molecular hydrogen. Most of the gas mass would be at this temperature, unless there is heating by photoionisation.

Higher mass loaded simulations extract the energy much more efficiently from the warm and hot phase. Therefore, the velocity widths as well as the energy extraction increase with mass loading. The overall cooling rate of the system was increased by about a factor of five for the low mass loaded simulations. For the high mass loaded simulations it was shown to increase further, whereas the quality of the simulations gets worse.

The simulations demonstrate the loss of numerical accuracy with increasing density contrasts. Three of the simulations conserve energy to a very good accuracy; further three have moderate problems, whereas the highest mass loading simulation has significant errors with respect to the

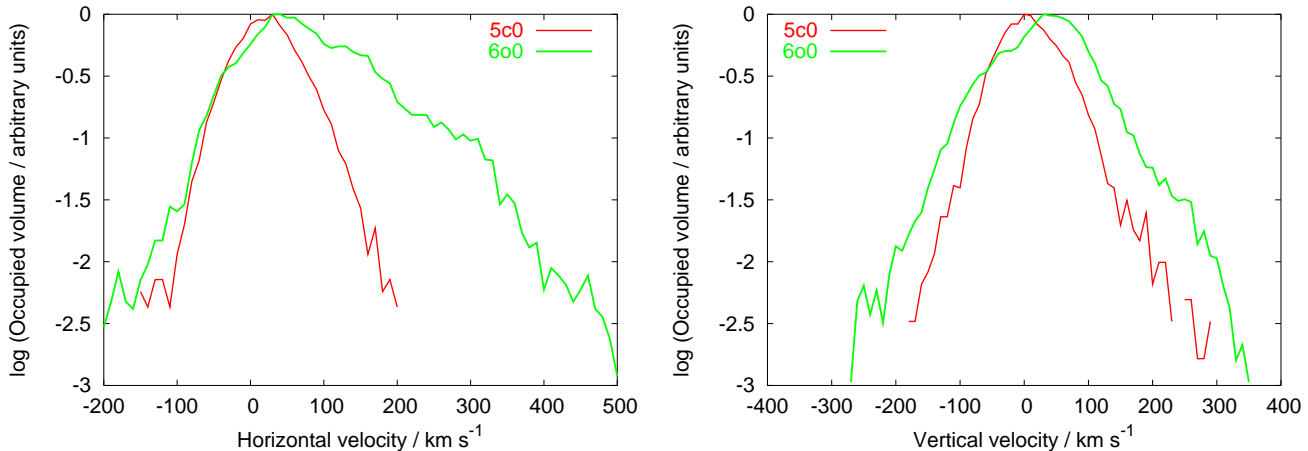


Figure 16. Velocity distribution functions for gas at temperature $14,000 \pm 2,000$ K for runs 5c0 and 6o0. Left: horizontal velocity. Right: vertical velocity. For better signal to noise, output between 1 and 6 Myr (0.1 Myr steps) has been staggered. The shift towards positive horizontal velocities, more pronounced for the higher mass load case is the result of the acceleration by the low density gas.

energy conservation. This is a clear trend. We conclude that the highest density contrast in a simulation is the limiting factor for numerical reliability. Despite these problems at extreme density ratios we believe the main trends and results are very reliable – we have checked this by comparing results to a high-resolution simulation performed using the FLASH code which is forced to be energy conserving.

The cold gas clouds effectively act as condensation nuclei. Strong growth of the cold gas mass is observed in all simulations which is in contrast to the control run in which no gas cools below 10^6 K for the whole simulation time. The lowest gas mass run, which is furthest from saturation, gains a factor of more than five in cold gas mass within 10 Myr. In a real radio cocoon the supply of warm gas would be ample, and exponential growth would result. Hence, a cold gas mass seed of order $100 M_\odot$ would be sufficient to condense the observed $\approx 10^9 M_\odot$ in the radio galaxies at $z \approx 1$ mentioned in the introduction, provided the conditions are similar to those considered here and if the typical source age is of order 100 Myr. It is worth noting that $\approx 10^9 M_\odot$ is also the amount of X-ray gas entrained into the radio cocoon as inferred from simulation (Krause 2005). A consistent picture emerges, if most of the entrained X-ray gas cools to the cold phase via the help of a small cold-gas seed. As this gas cools, most of the radiated energy is not in the X-ray band, but in the optical. Since in the real radio cocoon, unlike in the simulation here, the most energetic part of the system would be the radio emitting hot phase, a tight correlation between radio and optical emission would be expected, which is indeed observed (e.g. McCarthy 1993). Such a mechanism also of course explains the increased visibility of optically emitting regions after the passage of the radio cocoon.

Due to the large temperature ratios, heat conduction is a particular concern. However, it may still be negligible here, as we argue in the following. First, the evaporation lengthscale (Boehringer & Fabian 1989) is at least a factor of thousand below our resolution limit. Second, using Spitzer conductivity, we can estimate the energy transfer per volume due to heat conduction:

$$\dot{e} = \nabla \cdot [\sigma T^{2.5} \nabla T] \approx \frac{\sigma T^{3.5}}{dx^2} \approx 10^{-23} \text{ W m}^{-3} \left(\frac{T}{10^6 \text{ K}} \right)^{3.5}.$$

This leads to a heat conduction timescale of:

$$\tau_{\text{hc}} = \frac{e}{\dot{e}} \approx \frac{10^{-13} \text{ J m}^{-3}}{10^{-23} \text{ W m}^{-3} (T/10^6 \text{ K})^{3.5}} = 10^{10} \text{ s} \left(\frac{T}{10^6 \text{ K}} \right)^{-3.5}.$$

Since our simulations represent a dynamical equilibrium, we should compare this to the cooling timescale in order to find out to what extent heat conduction could contribute. The cooling time for the hot, warm and cold gas is of order 10^{20} s, 10^{15} s and 10^{11} s, respectively. So, heat conduction from the hot phase would clearly dominate everything else. However, in reality the presence of magnetic fields strongly suppresses heat conduction in and from the hot phase. If this was not the case, radio cocoons could not exist, since the internal energy would have been lost on the light crossing timescale. Among the cool gas, the heat conduction timescale is too long to be of concern. Therefore, we are left with the heat flow from the warm to the cold phase. Here, the heat conduction is about 10 times faster than the radiative cooling. For the simulation parameters, saturation sets in just above 10^6 K (?), and does therefore not influence the conclusion. However, also in the warm gas, the heat conduction is severely suppressed due to the presence of magnetic fields, at least for the current cosmological age. Measurements from X-ray data suggest a suppression by one to three orders of magnitude (Ettori & Fabian 2000; Markevitch et al. 2003; Nath 2003). The magnetic field in the warm gas around high redshift radio sources is unknown. However, if its effect on heat conduction is similar than in nearby cases, it will probably be a minor contribution to the total heat transfer. If the heat conduction would be less strongly suppressed, the processes described in this paper would be further amplified - more heat would be radiated by the cold phase and more warm gas would condensate on the cool gas.

The simulations presented here are 2D, only. This is an important first step, and it is very likely that the mechanisms we discuss would also be present in 3D – the Mach-number density relation is identical to published 3D results. To get more accurate estimates for example for cooling and mass dropout amplification or filling factors, 3D simulations are required. This is likely to be challenging, given the im-

portance of high resolution, but will no doubt be possible in the near future.

6 CONCLUSIONS

We presented 2D turbulence simulations initiated and driven only by the Kelvin-Helmholtz instability. We add dense, cooling clouds to the simulations, so that the interaction of the three phases present in the cocoons of high redshift radio galaxies may be examined. We find a turbulent cascade with energy spectrum proportional to $k^{-5/3}$ at larger scales, as in Kolmogorov turbulence. Mach number and density show a bimodal correlation with a break at a characteristic density, where the cooling time is about the simulation time. In the high density part, the Mach number goes as $\rho^{1/2}$, which is the same as found by independent 3D simulations by Kritsuk & Norman (2002). We use the relation to infer from the observed kinematics that either the density ratio in the high redshift sources is different from their low redshift counterparts or the temperature in the environment is lower. The temperature distribution function is dominated by a power law which we ascribe mainly to mixing. We find a strong peak in the distribution function at 14,000 K. This coincides with a strong rise in the cooling function, and corresponds to an equilibrium between shock heating and adiabatic compression on the one side and radiative cooling on the other side. We suggest that such gas is responsible for the optical emission in high redshifted radio galaxies, whenever shock ionisation dominates over photoionisation. We find a filling factor of 10^{-5} to 10^{-3} for the gas in this peak. The velocity width for this gas increases with mass load and is about 100 km/s for the simulations we consider to be reliable in this respect. By comparison of simulations with different loads of cold mass, we establish that the cooling time for the hotter phases is considerably reduced by the presence of the cold gas. We find an exponential growth of the cold mass with time due to cooling of warmer gas. The growth rate is sufficient to explain the origin of the optical gas associated with the cocoons of radio galaxies, as being build up by this turbulence enhanced cooling process. Heat conduction is not able to evaporate the cool clouds we inject. However, in cases where the suppression below the Spitzer value is less extreme than deduced from observations in nearby sources, it might contribute to the heat transfer significantly, and would presumably amplify the process we describe.

ACKNOWLEDGMENTS

We thank the referee for thorough reading of the manuscript and very helpful suggestions. MK acknowledges a fellowship from the Deutsche Forschungsgemeinschaft (KR 2857/1-1) and the hospitality of the Cavendish Laboratory, where this work has been carried out. The software used in this work was in part developed by the DOE-supported ASC / Alliance Center for Astrophysical Thermonuclear Flashes at the University of Chicago.

This paper has been typeset from a \TeX / \LaTeX file prepared by the author.

REFERENCES

- Alexander, P. 2002, MNRAS, 335, 610
 Alexander, P. & Pooley, G. G. 1996, in: *Cygnus A – Study of a Radio Galaxy*, ed. C. L. Carilli & D. E. Harris, Cambridge University Press, Cambridge, UK, 149
 Andreon, S., Valtchanov, I., Jones, L. R., Altieri, B., Bremer, M., Willis, J., Pierre, M., & Quintana, H. 2005, MNRAS, 359, 1250
 Arshakian, T. G. & Longair, M. S. 2004, MNRAS, 351, 727
 Bassett, G. M. & Woodward, P. R. 1995, ApJ, 441, 582
 Basson, J. F. 2002, Ph.D. Thesis, University of Cambridge
 Baum, S. A. & McCarthy, P. J. 2000, AJ, 119, 2634
 Best, P., Röttgering, H., Longair, M., & Inskip, K. 2000a, in *Emission Lines from Jet Flows*, ed. W. J. Henney, W. Steffen, L. Binette, & A. Raga, Instituto de Astronomia, Unam, Mexico
 Best, P. N. 2000, MNRAS, 317, 720
 Best, P. N., Carilli, C. L., Garrington, S. T., Longair, M. S., & Röttgering, H. J. A. 1998a, MNRAS, 299, 357
 Best, P. N., Eales, S. A., Longair, M. S., Rawlings, S., & Röttgering, H. J. A. 1999, MNRAS, 303, 616
 Best, P. N., Longair, M. S., & Roettgering, H. J. A. 1998b, MNRAS, 295, 549
 Best, P. N., Longair, M. S., & Roettgering, J. H. A. 1997, MNRAS, 292, 758
 Best, P. N., Longair, M. S., & Röttgering, H. J. A. 1996, MNRAS, 280, L9
 Best, P. N., Röttgering, H. J. A., & Longair, M. S. 2000b, MNRAS, 311, 1
 —. 2000c, MNRAS, 311, 23
 Bicknell, G. V. 1984, ApJ, 286, 68
 Boehringer, H. & Fabian, A. C. 1989, MNRAS, 237, 1147
 Calder, A. C., Fryxell, B., Plewa, T., Rosner, R., Dursi, L. J., Weirs, V. G., Dupont, T., Robey, H. F., Kane, J. O., Remington, B. A., Drake, R. P., Dimonte, G., Zingale, M., Timmes, F. X., Olson, K., Ricker, P., MacNeice, P., & Tufo, H. M. 2002, ApJS, 143, 201
 Carvalho, J. C. & O’Dea, C. P. 2002, ApJS, 141, 371
 Dey, A., van Breugel, W., Vacca, W. D., & Antonucci, R. 1997, ApJ, 490, 698
 Elmegreen, B. G. & Scalo, J. 2004, ARA&A, 42, 211
 Ettori, S. & Fabian, A. C. 2000, MNRAS, 317, L57
 Fanaroff, B. L. & Riley, J. M. 1974, MNRAS, 167, 31P
 Fryxell, B., Olson, K., Ricker, P., Timmes, F. X., Zingale, M., Lamb, D. Q., MacNeice, P., Rosner, R., Truran, J. W., & Tufo, H. 2000, ApJS, 131, 273
 Gilbert, G. M., Riley, J. M., Hardcastle, M. J., Croston, J. H., Pooley, G. G., & Alexander, P. 2004, MNRAS, 351, 845
 Hardcastle, M. J., Alexander, P., Pooley, G. G., & Riley, J. M. 1999, MNRAS, 304, 135
 Hippelein, H. & Meisenheimer, K. 1992, A&A, 264, 472
 Inskip, K. J., Best, P. N., Longair, M. S., & Röttgering, H. J. A. 2005, MNRAS, 359, 1393
 Inskip, K. J., Best, P. N., Longair, M. S., Rawlings, S., Röttgering, H. J. A., & Eales, S. 2003, MNRAS, 345, 1365
 Inskip, K. J., Best, P. N., Röttgering, H. J. A., Rawlings, S., Cotter, G., & Longair, M. S. 2002a, MNRAS, 337, 1407
 Inskip, K. J., Best, P. N., Rawlings, S., Longair, M. S., Cotter, G., Röttgering, H. J. A., & Eales, S. 2002b, MNRAS, 337, 1381

- Komissarov, S. S. 1990, *Astrophysics and Space Science*, 165, 313
- Kössl, D. & Müller, E. 1988, *A&A*, 206, 204
- Krause, M. 2005, *A&A*, 431, 45
- Krause, M. & Camenzind, M. 2001, *A&A*, 380, 789
- Kritsuk, A. G. & Norman, M. L. 2002, *ApJ*, 569, L127
- . 2004, *ApJ*, 601, L55
- Markevitch, M., Mazzotta, P., Vikhlinin, A., Burke, D., Butt, Y., David, L., Donnelly, H., Forman, W. R., Harris, D., Kim, D.-W., Virani, S., & Vrtilak, J. 2003, *ApJ*, 586, L19
- McCarthy, P. J. 1993, *A&AReview*, 31, 639
- Meisenheimer, K. & Hippelein, H. 1992, *A&A*, 264, 455
- Mellema, G., Kurk, J. D., & Röttgering, H. J. A. 2002, *A&A*, 395, L13
- Nath, B. B. 2003, *MNRAS*, 340, L1
- Neeser, M. J., Hippelein, H., & Meisenheimer, K. 1999, in *The Most Distant Radio Galaxies*, 467–+
- Neeser, M. J., Meisenheimer, K., & Hippelein, H. 1997, *ApJ*, 491, 522
- Norman, M. L., Winkler, K.-H. A., Smarr, L., & Smith, M. D. 1982, *A&A*, 113, 285
- Perley, R. A., Dreher, J. W., & Cowan, J. J. 1984, *ApJ*, 285, L35
- Puy, D., Grenacher, L., & Jetzer, P. 1999, *A&A*, 345, 723
- Saxton, C. J., Bicknell, G. V., & Sutherland, R. S. 2002, *ApJ*, 579, 176
- Shu, F. H. 1992, *Physics of Astrophysics*, Vol. II, University Science Books, Mill Valley, California
- Smith, D. A., Wilson, A. S., Arnaud, K. A., Terashima, Y., & Young, A. J. 2002, *ApJ*, 565
- Solórzano-Iñarrea, C., Best, P. N., Röttgering, H. J. A., & Cimatti, A. 2004, *MNRAS*, 351, 997
- Sutherland, R. S. & Dopita, M. A. 1993, *ApJS*, 88, 253
- Tavecchio, F., Maraschi, L., Sambruna, R. M., Urry, C. M., Cheung, C. C., Gambill, J. K., & Scarpa, R. 2004, *ApJ*, 614, 64
- Tegmark, M., Silk, J., Rees, M. J., Blanchard, A., Abel, T., & Palla, F. 1997, *ApJ*, 474, 1
- Ziegler, U. & Yorke, H. W. 1997, *Computer Physics Communications*, 101, 54